Korean J. Chem. Eng., 38(6), 1260-1271 (2021)
DOI: 10.1007/s11814-021-0816-2

pISSN: 0256-1115
eISSN: 1975-7220

Selective degradation of mixed dye pollutant in aqueous phase in the presence of ZnO/Al_2O_3 as sonophotocatalysis based on central composite design

Reza Mahdavi and Seyed Siamak Ashraf Talesh†

Department of Chemical Engineering, Faculty of Engineering, University of Guilan, Rasht, Iran
(*Received 31 December 2020 • Revised 20 April 2021 • Accepted 23 April 2021*)

Abstract−The selective sono/photocatalytic degradation of methyl orange (MO) in a mixture of methylene blue (MB) by synthesized ZnO/Al_2O_3 nanocomposites via ultrasound-assisted sol-gel method was studied. The synthesized samples were analyzed by XRD, TEM, EDX, BET, FTIR, UV-vis and Zeta potential analysis. The results showed that the ZnO nanoparticles were hexagonal wurtzite structures that changed to a flake-like quadrilateral morphology by enhancing the Al_2O_3 dosage. To optimize the selective removal efficiency of MO, response surface methodology (RSM) based on the central composite design (CCD) was applied to study the influence of Al_2O_3 dosage, catalyst amount, dye concentration and reaction time. A reliability prediction based on a second-order model was achieved with a high coefficient of determination (R^2) and adjusted R^2 of 0.9914 and 0.9834 for the optimized removal process, respectively. The MO optimal conditions of selective removal efficiency were found at 6.39 wt% of Al_2O_3 dosage, 32.2 mg catalyst amount, 7 mg/L of dye concentration and reaction time of 150 min to achieve 91.42% removal of MO dye. In the optimal conditions of selective removal, the advanced sono/photocatalytic technique was used to investigate the complete degradation of the adsorbed MO on the catalyst surface. The FTIR spectrum of the MO degradation shows complete removal of some bands compared to the initial control dye, which confirms the degradation of MO after ultrasonic (US) and ultraviolet (UV) irradiation. The use of ZnO/Al_2O_3 nanocomposites in sonocatalysis process leads to producing electron/hole pairs, whereby the production of reactive oxygen species, MO selected molecules were oxidized quickly.

Keywords: Selectivity, Sonocatalytic, Methyl Orange, Experimental Design, Optimization

INTRODUCTION

Wastewater treatment in the chemical industries is one of the largest and most complex industrial problems in the manufacturing sector [1]. Dye compounds constitute a significant part of the chemical wastewater. The wastewater entering the environment can cause various diseases such as hypertension, respiratory disorders, aquatic organisms and plant death [2]. Treatment methods of these materials are divided into three biological, physical and chemical groups [3]. These methods include adsorption [4], filtration [5], sedimentation [6], Fenton [7], wet air oxidation [8] and electrochemical methods [9]. The use of these methods aimed to remove dye pollutants is problematic due to secondary pollution, corrosion of transfer pipes, the formation of hazardous products and biological behaviors [10]. In recent years, new advanced oxidation methods based on the production of hydroxyl radicals have been considered for water and pollutant treatment. Hydroxyl radicals can be produced through the direct decomposition of water using an external energy source (ultraviolet, visible and ultrasound) [11]. Combining photocatalysis with other oxidation methods including sonocatalysis has shown to be a very efficient technique for treating wastewater [12]. When the ultrasound passes through the solution, the local pressure difference produces microbubbles leading to producing vibrational energy and making the system unstable. These bubbles produce powerful energy at high temperature and pressure, which degrades water molecules into hydroxyl radicals [13]. The ultrasound applications are based on physical effects, such as cavitation and micro-jet phenomena and in some cases based on chemical effects, such as the production of free radicals in solution [14]. The final mechanism of both photocatalytic and sonocatalytic processes results in electron-hole excitation and the formation of hydroxyl radicals. Sonocatalysts and photocatalysts are highly dependent on the catalyst type. These are usually composed of nanoparticles such as TiO_2, ZnS, ZnO, Fe_2O_3, SnO_2, WO_3 and CdS, which are activated under light or ultrasound irradiation [15,16].

Recently, nanoparticle synthesis techniques based on the ultrasound irradiation have been significantly developed. The nanostructure properties synthesized by the sol-gel method can be improved using ultrasound during the hydrolysis process of raw materials (the initial stage of the sol-gel process) [17]. A reduction in synthesis time from a few days to several hours, more uniform particle size distribution, activation of the particle surface, optimal use of energy, higher surface area, ability to create a homogeneous coating of nanoparticles on various surfaces and enhanced phase purity are significant advantages of this method [18,19]. The mechanism of formation and growth of nanoparticles is accomplished at three general stages using the sonochemical method [20]: 1) nucleation, whereby the reaction between the raw materials results in the formation of primary nuclei, by the application of ultrasound, 2) growth, which the raw materials diffuse the surface of the primary nucleus and, upon reaction, precipitates on its surface and attaches to it and 3) reaching the desired size and separating it from the solution con-

†To whom correspondence should be addressed.
E-mail: s_ashraf@guilan.ac.ir

taining raw materials, to prevent increasing nanoparticle size and controlling the properties.

The selective sono/photocatalysts are becoming an important research topic in the field of advanced catalysts. Selectivity is significant for a mixture that contains compounds that should be recovered [21]. Non-selective behavior becomes a more serious problem when the catalyst cannot distinguish between hazardous and non-hazardous compounds. Nanoparticles non-selective property is a major defect as photocatalysts or sonocatalysts which limits their application in treatment systems. At non-selective catalyst condition, the catalyst surface absorption capacity may be saturated by other organic matter at higher concentrations of wastewater. This is apparently the necessity for the development of selective catalysts.

Liu et al. [22] used ZnO nanoplates coated with ethylene glycol as a new photocatalyst for selective degradation of MO and RhB dyes. They synthesized porous ZnO nanoparticles by changing the crystalline structure of the particles and utilizing the selective properties of the porous particles to absorb rhodamine dye. Pakdel et al. [23] prepared TiO_2/SiO_2 nanoparticles as a new photocatalyst for selective removal of MB and MO. According to their research, when SiO_2 nanoparticles are synthesized by the Co-precipitation method in TiO_2/SiO_2 composite, the tendency to adsorb MB dye will increase. Jose et al. [24] studied selective activity using the TiO_2 nanoparticles separation technique from a colloidal solution. This study indicated that the surface charge of nanoparticles was changed using acidic and alkaline compounds during the synthesis process to absorb the selective pollutant into the catalyst and degraded the selective pollutant by the photocatalytic process. Ye et al. [25] investigated the photocatalytic selective degradation of MO and MB dyes using TiO_2 nanoparticles, which resulted in 50% selectivity of MB. Zhang et al. [26] reported the selective removal of MO in a mixture of MB and MO using TiO_2 nanoparticles in the presence of UV radiation. Lazar et al. [27] investigated the selective degradation of MO and MB using modified TiO_2 nanoparticles with different surface charges. In most research, TiO_2 nanoparticles have been used as selective catalysts and, so far, to the best of our knowledge, have not been performed in any study regarding selective degradation of ZnO/Al_2O_3 catalysts using sono/photocatalytic technique.

The literature review shows few studies conducted on the heterogeneous catalysts selectivity improvement under ultrasound. By controlling the process of adsorption and degradation of organic compounds, photochemical and sonochemical processes can be the most beneficial and economical method to obtain valuable compounds. The use of the adsorption method may cause desorption phenomenon and secondary pollution. In the present research, to solve this challenge, ZnO/Al_2O_3 nanocomposites with high adsorption and oxidation performance were synthesized and modified using sonochemical process. The structure, morphology and absorption spectra of samples were characterized using XRD, TEM and UV-Vis spectroscopy, respectively. Optimization and effects of experimental parameters on selective removal of MO mixed with MB were investigated by the central composite design (CCD) method.

EXPERIMENTAL

1. Materials and Methods

ZnO/Al_2O_3 catalyst was prepared by an ultrasound-assisted sol-gel method. Zinc acetate ($Zn(CH_3COO)_2{\cdot}2H_2O$) and aluminum nitrate ($Al(NO_3)_3{\cdot}9H_2O$) solution were used as starting materials. Zinc acetate was dissolved in distilled water to prepare a 0.3 M solution and then NaOH aqueous solution was added dropwise into the zinc acetate. Subsequently, an ultrasound wave was irradiated at the power of 300 W and a frequency of 20 kHz for 30 min. The resulting white product was washed with deionized water and ethanol, centrifuged and dried in the oven at 100 °C for 2 h. Depending on the required concentration of Al_2O_3, the corresponding amount of aluminum nitrate was added to the solution of zinc acetate. MO and MB were selected as a pollution source. All the materials were bought from Merck Company. Their characteristics and molecular composition are depicted in Fig. 1 [28].

2. Catalyst Characterization

X-ray diffraction (XRD) patterns for different samples were characterized using a Philips PW 1730 X-ray diffractometer with Cu Kα radiation source. The surface morphology and particle size of catalysts were examined by a transmission electron microscopy (TEM- Philips EM208S). The compositional analysis of catalysts was examined with an energy dispersive X-ray spectrometer (EDX-TESCAN MIRA). Fourier transform infrared spectrometer (FTIR-

Characteristic	Methyl orange	Methylene blue
Structure	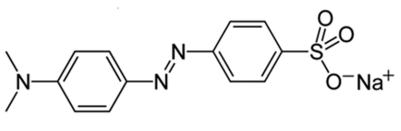	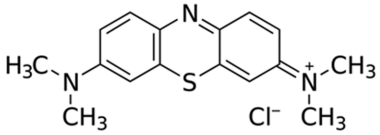
Chemical formula	$C_{14}H_{14}N_3NaO_3S$	$C_{16}H_{18}N_3SCl$
Molar mass	327.33 g.mol^{-1}	319.85 g.mol^{-1}
Appearance	Orange solid	Dark green solid
Density	1.28 g/cm^3	1.757 g/cm3
Solubility in water	0.5 g/100 mL	4.36 g/100 ml

Fig. 1. The chemical formula and molecular structure of methylene blue and methyl orange.

Thermo AVATAR) was applied at room temperature to determine the specific functional groups. Zeta potential (Zeta- HORIBA Scientific SZ-100) analysis was used to identify and determine the particle surface charge. The absorption spectrum of nanoparticles and dye contaminants was investigated by spectrophotometer UV-Vis (Varian- Cary 50 Bio).

3. Experimental Method

To study the selective performance of the synthesized catalysts, 50 mL of anionic/cationic dye mixture (MO/MB) was prepared in different concentrations. Then the ZnO/Al_2O_3 catalyst was added to the prepared mixture. The formed suspension was stirred for a specified time to ensure equilibrium adsorption and desorption. During this time, the anionic dye (MO) absorbs to the catalyst surface due to the positive surface charge of the nanoparticles. After that, dye concentration was measured with a UV-vis spectrophotometer. The CCD method was applied to optimize the experimental conditions to achieve maximum removal. The experimental parameters for performing this experiment are summarized in Table 1. The degradation begins with the initiation of radiation processes (UV and US). An ultrasonic bath (JPL Ultra 8060, frequency of 20 kHz and power of 200 W) and a UV lamp (Hg lamp mercury Italy, power of 6 W) were irradiated to the organic dye solution. The steps of this experiment are presented schematically in Fig. 2. Selective removal was calculated by Eq. (1) and (2).

Table 1. Experimental conditions and levels of the independent variables

Sample	S_{BET} (m^2/g)	V_t (cm^3/g)
ZnO	14.13	0.11
ZnO/Al_2O_3	89.53	0.23

$$\text{Removal \% } (R)=(C_0-C)/(C_0)\times 100 \quad (1)$$

$$\text{Selective removal\% } (S)=(R_{anion})/(R_{cation}+R_{anion})\times 100 \quad (2)$$

C_0 is the initial dye concentration and C is the final dye concentration. R_{anion} and R_{cation} are the removal rates of anionic and cationic dyes, respectively.

4. Experimental Design and Statistical Analysis

The RSM method was used for process optimization and exper-

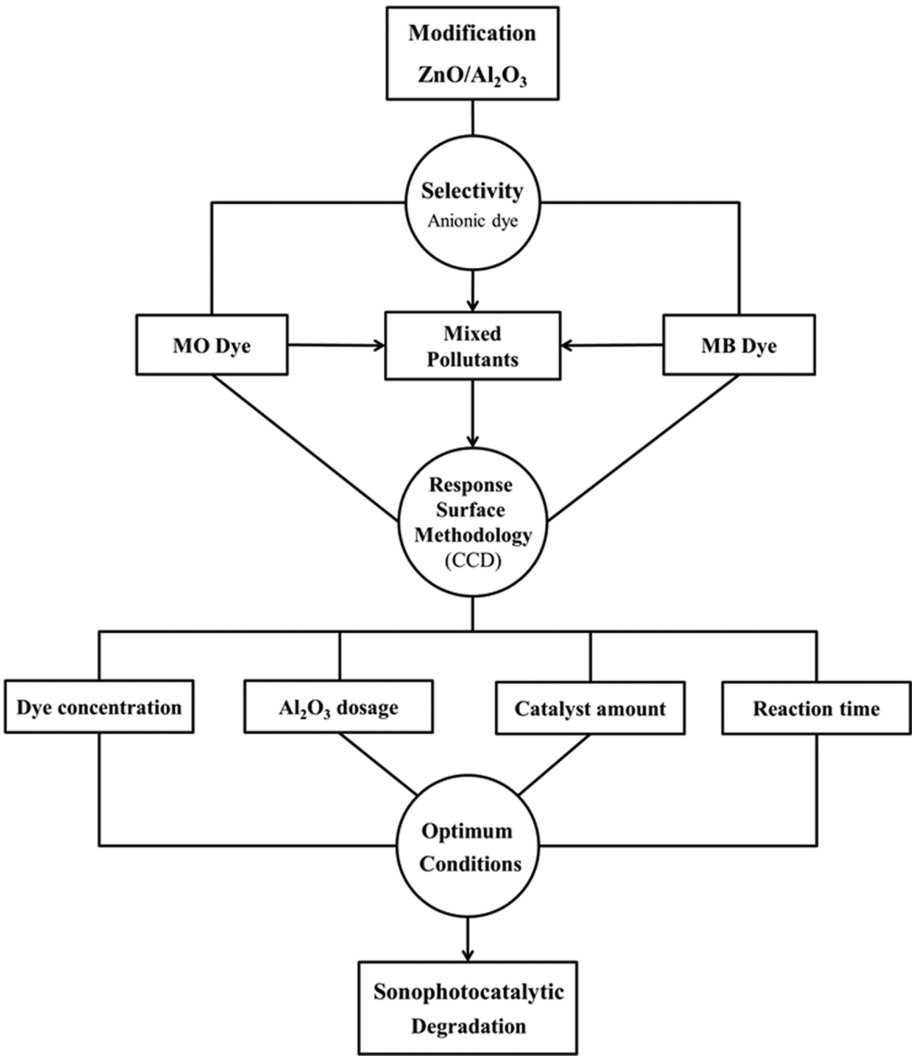

Fig. 2. The steps of selective sonophotocatalytic degradation experiment.

Table 2. CCD matrix of experimental values and predicted values for selective removal of MO

Central composite design (CCD)			
Factors	Units	Ranges	
Al_2O_3 dosage	%wt	1	9
Catalyst amount	mg	10	50
Dye concentration	mg/L	7	15
Reaction time	min	30	150

imental design. The RSM method based on the CCD technique is well matched for fitting a quadratic and process optimization. A set of 30 experiments were designed to optimize the selective removal of MO by ZnO/Al_2O_3 catalyst. The six replications were done at the center point to supply information on the responses variation of the average and the residual variance. The four selected independent variables were the Al_2O_3 dosage (A), catalyst amount (B), initial concentration of dye (C) and reaction time (D). The selective removal of MO was selected as the output parameter (response). The levels and ranges of experimental variables were specified through a series of preliminary experiments (Table 1). Alpha parameter value ($\alpha=(n)^{1/4}$, where n is the number of parameters) for the rotatable design was fixed at 2. The value of α illustrates design rotatability, which depends on several variables, was used in the experiment [29]. Table 2 shows the experimental response and experiment matrix. The experimental response can be approximated with the second-order polynomial (Eq. (3)) [30].

$$Y = b_0 \sum_{i=1}^{k} b_i X_i + \sum_{i=1}^{k} b_{ii} X_i^2 + \sum_{i=1}^{k} \sum_{j>1}^{k} b_{ij} X_i X_j + \varepsilon \quad (3)$$

where, Y is the predicted response, X is the independent variable, b_0 is the constant coefficient, b_i, b_{ii} and b_{ij} are the regression coefficients of linear, quadratic and the second-order terms, respectively, and ε is the error.

RESULTS AND DISCUSSION

1. Catalyst Characterization

1-1. Crystallography and Morphology

The XRD patterns of the synthesized samples are shown in Fig. 3. According to this figure, the hexagonal and wurtzite crystalline phase of ZnO was revealed corresponded by the Joint Committee on Powder Diffraction Standards data (JCPDS, 36-1451). No impurities of $Al(OH)_3$ or $Zn(OH)_2$ were observed. The results clarify that no additional peaks correspond to the Al_2O_3 phase, when the dosage of the Al_2O_3 is fixed from 0 to 9 wt%. By increasing of Al_2O_3 dosage, the peaks widening and shift towards higher values of the X-ray diffraction angle were observed with the enhancement of Al_2O_3 dosage. Average crystal size was obtained by Scherrer's formula (Eq. (4)) [31]:

$$D = \frac{K\lambda}{B\cos\theta} \quad (4)$$

where D is average crystallite size (nm), k is a constant of Scherrer equation (0.9), λ is the wavelength of Cu Kα radiation (0.15406 nm), B is the full-width at half maximum of height and θ is the angle of the X-ray. According to Scherrer's equation, when Al_2O_3 dosage increases from 0 to 9%, the crystallite size decreases. This revealed that a small dosage of Al_2O_3 has a significant influence on the crystal size.

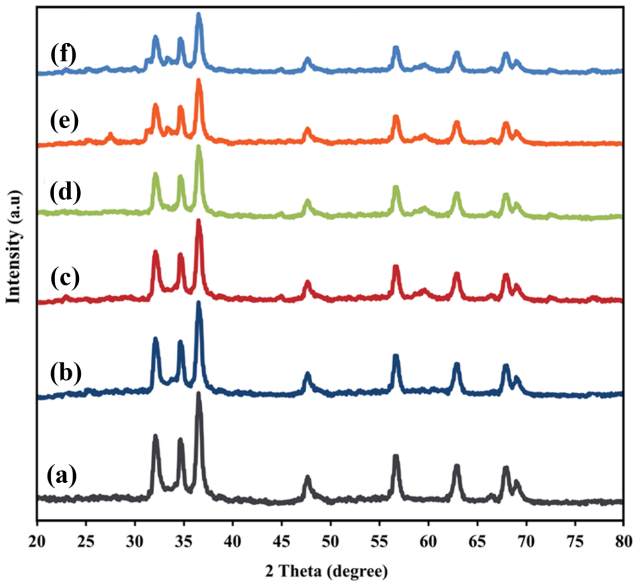

Fig. 3. The X-ray diffraction patterns of Pure ZnO (a), 1% Al_2O_3 (b), 3% Al_2O_3 (c), 5% Al_2O_3 (d), 7% Al_2O_3 (e) and 9% Al_2O_3 (f).

To characterize the morphological property of Al_2O_3/ZnO nanocomposites, the TEM images are shown in Fig. 4. Fig. 4(a) represents that the Pure ZnO catalyst comprises small particles with a hexagonal polyhedral structure and a diameter of 50 to 100 nm. Fig. 4(b) and (c) illustrate the effect of 5% and 9% Al_2O_3 dosage on ZnO particle morphology, respectively. According to these figures, the as-synthesized samples are flake-like quadrilateral mor-

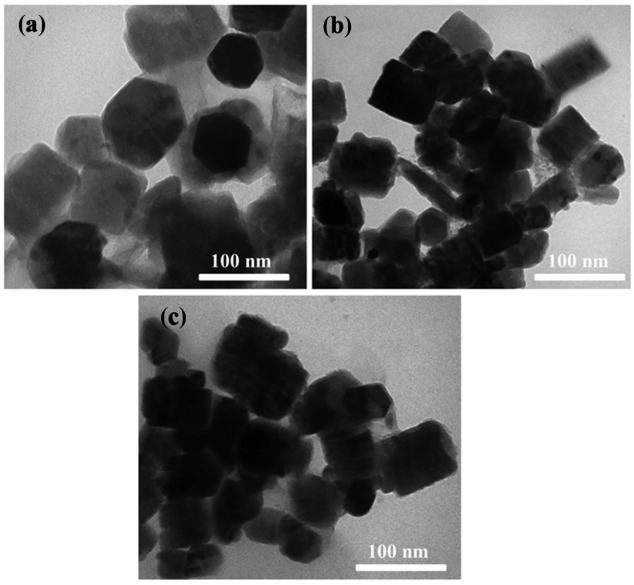

Fig. 4. TEM images of pure ZnO (a), 5% Al_2O_3 (b), and 9% Al_2O_3 (c) nanocomposites.

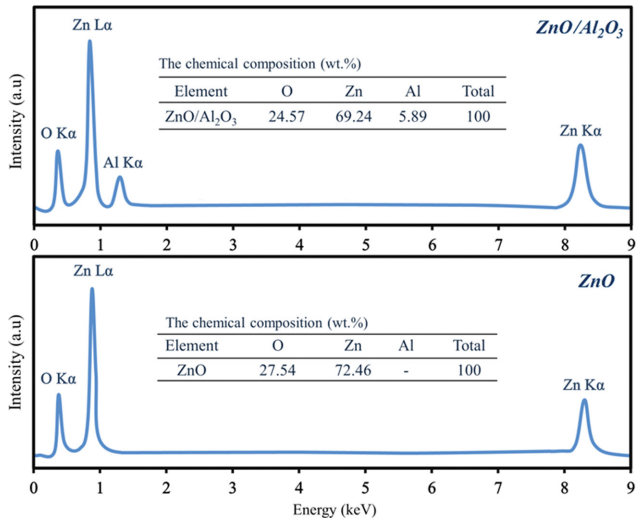

Fig. 5. EDX spectra and elemental compositions of pure ZnO and ZnO/Al_2O_3.

phology and the length and diameter are 50-100 nm. It was revealed that by an increment of Al_2O_3 amount, the particles are agglomerated and the hexagonal morphology of ZnO nanoparticles changes to flake-like quadrilateral morphology. Fig. 5 shows the EDX spectra and elemental composition of pure ZnO and ZnO/Al_2O_3 (6.39 wt% Al_2O_3) nanoparticles. The EDX spectrum of the ZnO/Al_2O_3 displays a clear Al Kα line at 1.3 keV, which is evidence of the presence of Al_2O_3 compounds. No traces of other elements were found in the spectrum, which confirms the purity of the samples. Moreover, atomic percentage of Zn, Al, and O for ZnO and ZnO/Al_2O_3 samples shows the actual concentration of Al is found to be 5.89 wt% for the sample of 6.39 wt% ZnO/Al_2O_3.

1-2. Zeta Potential and BET Analysis

The zeta potential is an important criterion to analyze the possible interaction between nanoparticles and dye molecules. Zeta potential was measured on synthesized catalysts to investigate the surface charge of the nanoparticles, as is shown in Fig. 6. In this measurement, ZnO/Al_2O_3 (+35 mV) presents a positive surface

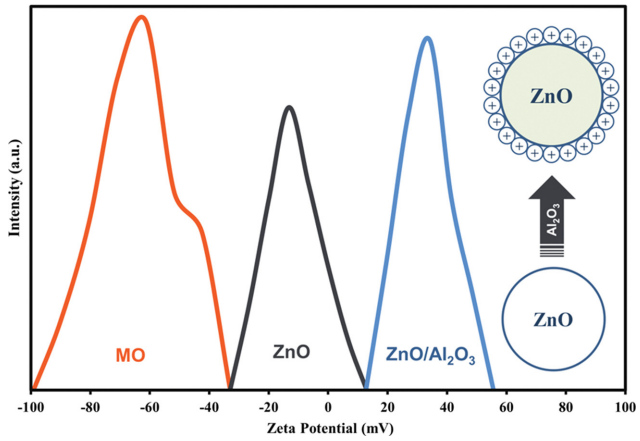

Fig. 6. The zeta potential analysis of the methyl orange, ZnO and the ZnO/Al_2O_3 nanocomposites.

charge while ZnO (−16 mV) and MO dye (−62 mV) demonstrated a negative surface charge. The considerable positive value of zeta potential indicates the presence of positively charged functional groups on the surface of the catalysts. As revealed by the zeta potential results, the Al_2O_3 particles cause increments of the efficiency of the adsorption process in the electrostatic interactions between MO and ZnO nanoparticles [32]. The BET surface area and total pore volume of synthesized catalysts are listed in Table 3. By combining Al_2O_3 support and ZnO nanoparticles, the BET surface area and total pore volume of the composite was increased in comparison to pure ZnO. Therefore, the textural properties of ZnO/Al_2O_3 are greater than the pure ZnO nanoparticles. This result confirms that using the ZnO/Al_2O_3 composite can represent better efficiency in selective removal due to its higher surface area and pore volume.

2. Statistical Analysis of Selective Removal

The selective removal of MO was found in the range of 38.45 to 85.35%. A regression analysis was carried out to fitting the experimental response and predicted values. The approximating function of selective MO obtained by the CCD method is given in Eq. (5):

$$\%\ \text{Selective removal} = +75.42 + 5.74\,A + 10.98\,B - 4.42\,C + 4.27\,D - 0.18\,AB - 0.33\,AC + 0.096\,AD + 2.54\,BC - 2.03\,BD - 0.54\,CD - 4.71\,A^2 - 3.89\,B^2 - 0.92\,C^2 - 0.92\,D^2 \quad (5)$$

Positive and negative signs in Eq. (5) illustrate the efficacy of the synergistic and antagonistic, respectively. Table 2 indicates the predicted values using the second-order model, which are in good correspondence to the experimental values. Table 4 represents the ANOVA results. The significance of the model was assessed based on the coefficient of determination (R^2). The R^2 value achieved 0.9914, which is relatively high. This means that 99.14% of the variations for the selective removal of MO are expressed by the independent variables and only 0.86% of the total variation is not included in the response [33]. A high R^2 indicates that the obtained model provides a good estimate of the response in the studied range. Moreover, the large amount of adjusted R^2, obtained as 0.9834, represents a high correlation between the experimental and predicted data. The F-value of 23.92 reveals that the model was reliable for the selective removal of MO. The adequate precision, which indicates the signal to noise ratio, was measured greater than 4 (equal to 39.76), which is acceptable [34]. The lack of fit F-value and P-value was obtained 3.85 and 0.075, respectively, confirming that the model of the selective removal of MO is reliable. The non-significant lack of fit represents the good accuracy of the model [35]. The low CV values indicate high accuracy and validity of the experiments, which reached 2.69 in this research [36]. Accordingly, the high R^2 value, significant F-value model, non-significant P-value of lack-of-fit and low CV illustrate good predicting the MO removal. Therefore, these models were used for further analysis. As shown in Table 5, the coefficient's significance for the removal of MO was specified by F and P-values.

The normal probability graph (Fig. 7(a)), the plots of residual vs. predicted values (Fig. 7(b)) and the Box-Cox graph (Fig. 8) confirm the model compatibility. This confirms that the developed model is appropriate for predicting the selective removal of MO. The residual values near the straight line show the adaptability of the model to depict the relation between the response and the

Table 3. BET surface area and total pore volume of ZnO pure and optimal catalyst

Run order	Actual parameters				Selective removal of MO		
	A	B	C	D	Experimental (%)	Predicted (%)	Residls
1	7	20	9	60	59.49	60.26	−0.77
2	7	40	9	60	81.36	80.84	0.52
3	5	30	15	90	62.27	62.89	−0.62
4	5	30	11	90	75.44	75.42	0.018
5	3	20	13	60	37.12	35.79	1.33
6	5	30	11	30	60.28	63.18	−2.90
7	5	50	11	90	81.31	81.81	−0.50
8	9	30	11	90	70.11	68.07	2.04
9	3	40	9	60	70.85	69.25	1.60
10	5	30	11	90	76.12	75.42	0.70
11	7	20	9	120	72.91	74.13	−1.22
12	1	30	11	90	43.15	45.13	−1.98
13	5	30	11	90	76.47	75.42	1.05
14	7	40	9	120	85.35	86.60	−1.25
15	3	40	13	120	71.32	70.46	0.86
16	5	30	11	90	74.11	75.42	−1.31
17	3	40	9	120	73.58	74.63	−1.05
18	5	30	11	90	74.14	75.42	−1.28
19	7	20	13	60	47.67	46.76	0.91
20	7	40	13	120	80.09	81.11	−1.02
21	5	30	7	90	81.25	80.56	0.69
22	5	30	11	90	76.25	75.42	0.83
23	3	20	9	120	61.32	61.45	−0.13
24	5	10	11	90	38.45	37.89	0.56
25	3	40	13	60	68.32	67.24	1.08
26	7	40	13	60	77.72	77.51	0.21
27	7	20	13	120	56.96	58.47	−1.51
28	3	20	13	120	46.45	47.11	−0.66
29	5	30	11	150	83.23	80.27	2.96
30	3	20	9	60	48.84	47.97	0.87

A: Al_2O_3 dosage (%wt); B: Catalyst amount (mg); C: Dye concentration (mg/L); D: Reaction time (min)

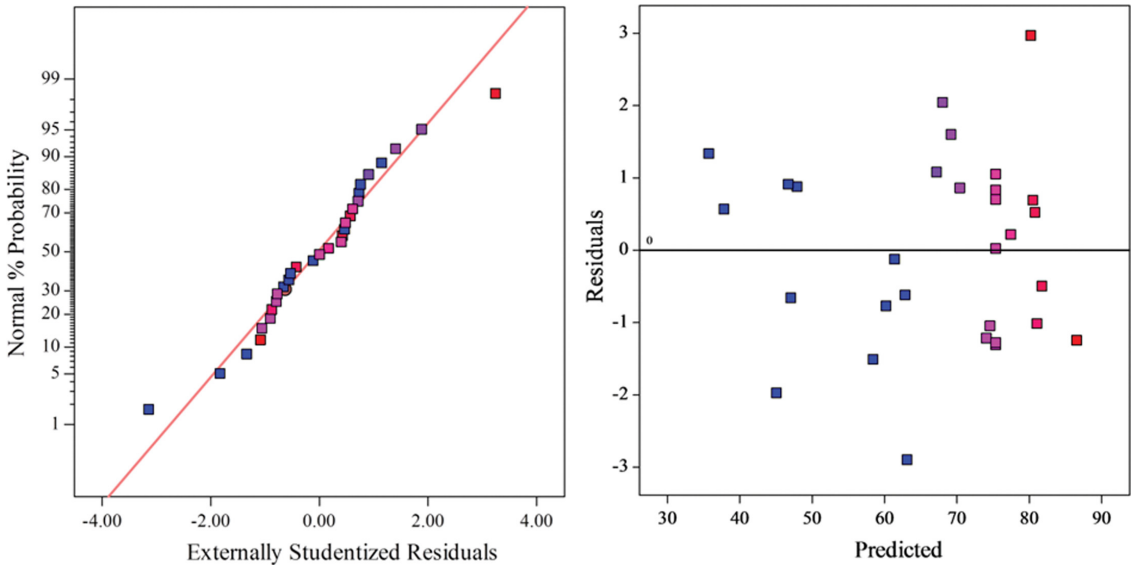

Fig. 7. The graphical normal probability plot (a) and residual vs. predicted values (b).

Table 4. ANOVA results for selective removal of MO in MB/MO mixture

Model	R^2	Adjusted R^2	Predicted R^2	RMSE	Adeq. precision	F-value	P-value	Lack of fit	S.D	C.V
Quadratic	0.9914	0.9834	0.9549	1.81	39.76	123.92	<0.0001	0.075	1.81	2.69

Table 5. Coefficient estimate, F-values and P-values for selective removal of MO in MB/MO mixture

Factor	Selective removal of MO		
	Coefficient estimate	F-value	p-value
A	5.74	241.83	<0.0001
B	10.98	886.25	<0.0001
C	−4.42	143.39	<0.0001
D	4.27	134.08	<0.0001
AB	−0.18	0.16	0.6989
AC	−0.33	0.54	0.4755
AD	0.096	0.045	0.8352
BC	2.54	31.66	<0.0001
BD	−2.03	20.13	0.0004
CD	−0.54	1.43	0.2511
A^2	−4.71	185.99	<0.0001
B^2	−3.89	127.31	<0.0001
C^2	−0.92	7.16	0.0173
D^2	−0.92	7.18	0.0172

A: Al_2O_3 dosage (%wt); B: Catalyst amount (mg);
C: Dye concentration (mg/L); D: Reaction time (min);

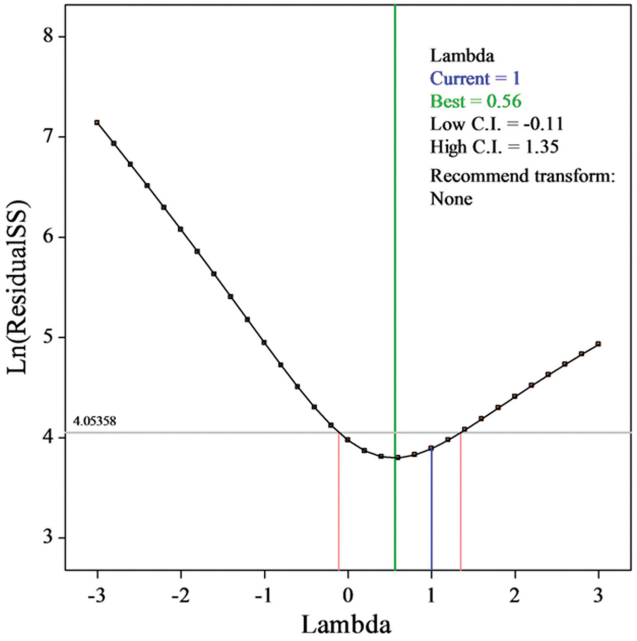

Fig. 8. The plot of Box-Cox transformation.

independent variables [37]. Fig. 7(b) shows the random scattering of the residual values and distribution between −3 and +3. Finally, the good prediction of the model was verified by the Box-Cox graph (Fig. 8), where no transformation was recommended for the model.

For better explanation of the CCD results, Pareto analysis was considered. As shown in Fig. 9, the Bonferroni limit line (3.273)

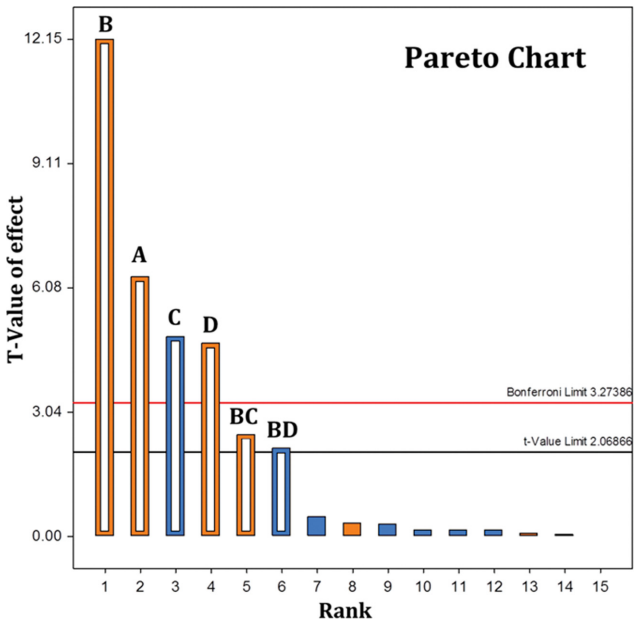

Fig. 9. Pareto chart analysis to determine the effectiveness of each variable.

and t-value limit line (2.068) were determined. In Pareto chart, the significance of coefficients statistically is classified into three categories. The first coefficient with t-value of the effect above the Bonferroni limit is called certainly significant. The second coefficient with t-value of the effect between Bonferroni line and the t-value limit line is termed as possibly significant, and the third one with t-value of the effect below the t-value limit line is named insignificant coefficient [38]. The Pareto chart indicates that the catalyst amount (B), Al_2O_3 dosage (A), dye concentration (C), and reaction time (D) represented highly affecting (certainly significant) the selective removal of MO, respectively. Moreover, the influence of Al_2O_3 dosage, catalyst amount and reaction time on coefficient is positive, whereas it is negative for dye concentration.

2-1. Effect of Independent Parameters

A perturbation diagram compares the effect of all four parameters together on the selective removal of MO at a specific point in the design space (Fig. 10). The output variable is designed by changing only one parameter within its range, while the other parameters are fixed. According to Fig. 10, Al_2O_3 dosage (A), catalyst amount (B), dye concentration (C), and reaction time (D) are the controlling variables to achieve maximum selective removal of MO. The MO anionic ions can be adsorbed on the active sites of ZnO/Al_2O_3 with a positive charge. The active surface charge of ZnO nanoparticles is created by the formation of polar surfaces and the asymmetric structure of Al_2O_3 [39]. Moreover, Al_2O_3 particles with a high surface area have a considerable role in enhancing the adsorption of ZnO nanoparticles. In Fig 10, by increasing the Al_2O_3

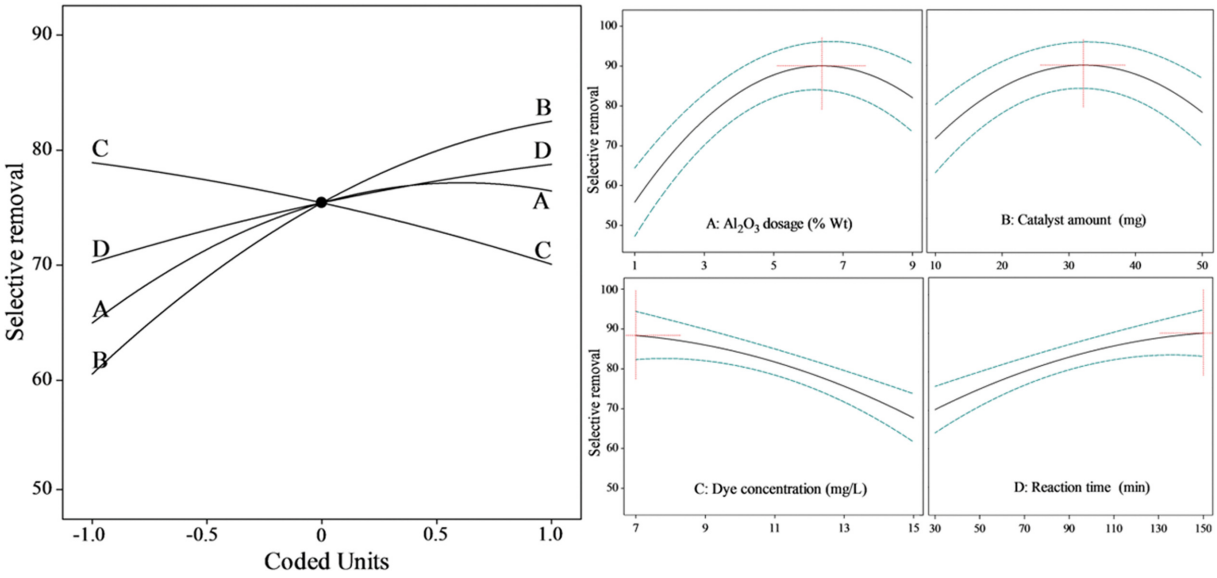

Fig 10. Perturbation plot and the main effect of Al_2O_3 dosage (A), catalyst amount (B), dye concentration (C) and reaction time (D).

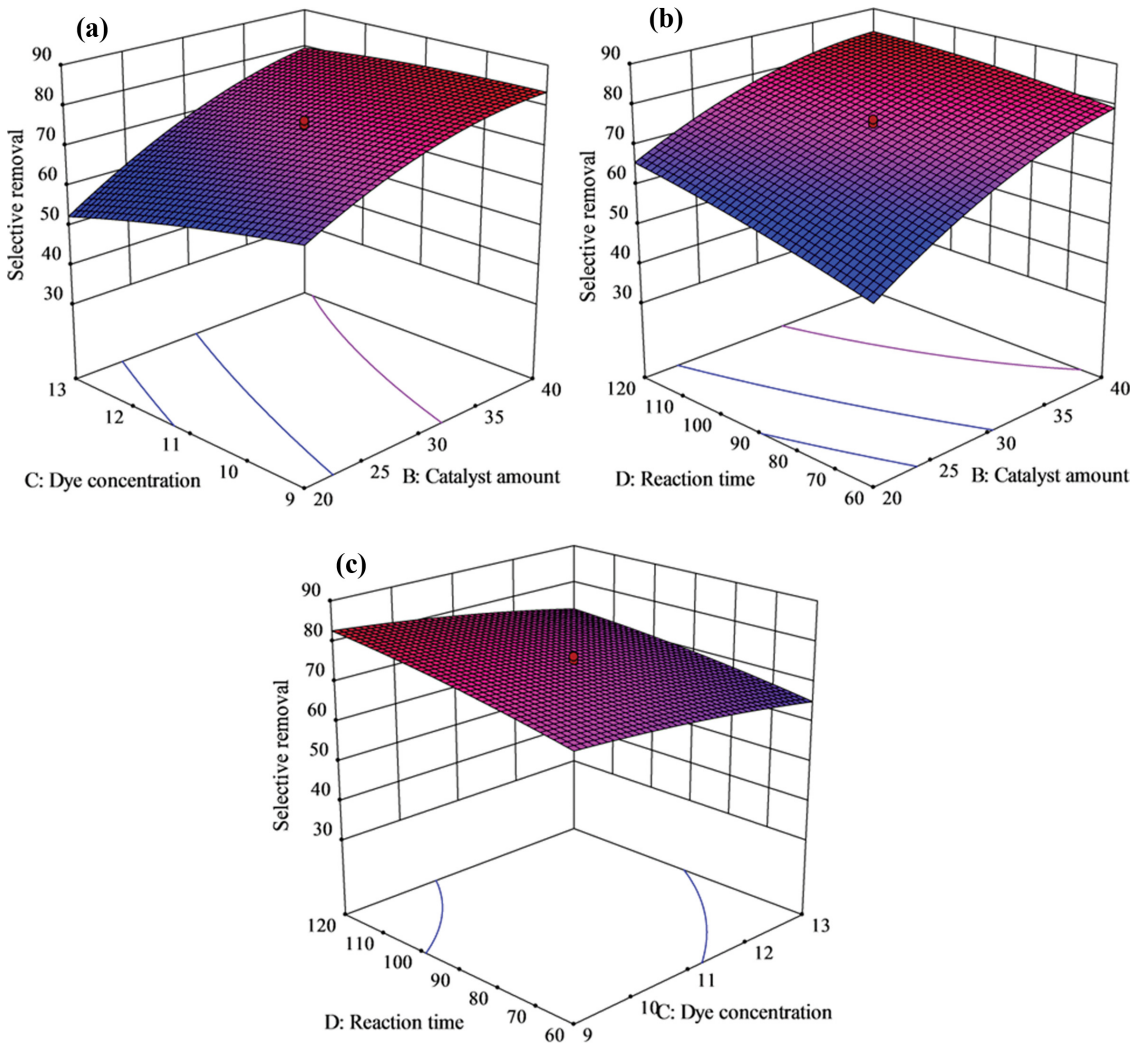

Fig. 11. Three-dimensional plots of interactive effects between (a) catalyst amount and dye concentration, (b) catalyst amount and reaction time and (c) dye concentration and reaction time on selective removal.

dosage, due to the higher positive charge of the Al_2O_3 surfaces, the adsorption capacity of the particles increased and higher adsorption of MO was observed. By enhancement of Al_2O_3 dosage, the selective removal increases to a specific value and then decreases. Due to more ZnO/Al_2O_3 particles, the MO removal efficiency increases because of the greater accessibility of more adsorption sites and adsorbent surface [40]. Furthermore, an enhancement in catalyst amount simplifies the access of MO molecules to adsorption sites due to more active sites. Moreover, as the initial MO concentration increases, the slope of the MO concentration between the dye aqueous and the solid phase increases. Finally, it acts as a driving force to the transition of MO molecules to the adsorbent surface [41]. It can be concluded that selective removal was reduced with an enhancement in dye concentration. The intense dye molecule adsorption on the surface of the catalysts causes a significant reduction in selectivity efficiency due to the dye concentration increasing. The contact time of absorbent with dye solution is one of the significant influential variables on selectivity performance. Consideration of the reaction time effect on process efficiency is demonstrated in Fig 10. A direct correlation between contact time and removal rate can be seen in this figure. According to the results, the highest selectivity was obtained for the MB/MO mixtures at 150 min.

2-2. Interaction of Operational Parameters

Fig. 11(a) illustrates the three-dimensional (3D) response surface plot of selective removal at 5 wt% of Al_2O_3 dosage and reaction time 90 min, to investigate the interaction between MO concentration and catalyst amount. At various catalyst amounts, the selective removal was decreased with initial concentration increasing. At the beginning of the process, the high concentration may cause excessive adsorption of MO molecules on the catalyst surface. The response surface plot of selective removal at Al_2O_3 dosage of 5 wt% and concentration of dye 11 mg/L with a different catalyst amount and reaction time are indicated in Fig. 11(b). The effect of catalyst amount was more significant at high reaction time. The selective removal increased slightly by an increment of catalyst amount from 10 to 40 mg and then decreased slightly at a higher amount. Moreover, it showed a detrimental effect as too much dosage of the catalyst was added. Fig. 11(c) represents the interaction between dye concentration and reaction time in the 3D response surface plot at Al_2O_3 dosage 5 wt% and 30 mg of catalyst amount. The dye concentration has a higher effect on the selective removal at high reaction time than at short reaction time.

2-3. Optimization

Numerical optimization was used to specify the optimal values for the maximum selective removal. The optimal conditions for the selective removal of MO in mixtures are shown in Fig. 12. As a result, the maximum selective removal of 90.06% was achieved at the Al_2O_3 dosage of 6.39 wt%, catalyst amount of 32.2 mg, dye concentration of 7 mg/L, and reaction time of 150 min. To confirm the results obtained from the CCD, experiments were performed at the optimum condition, which rate of selectivity was achieved equal to 91.42%. This result confirmed the validity of the applied model for predicting selective removal.

The absorption spectrum of MO removal in the mixture with MB at the optimum conditions is presented in Fig. 13. Appling ZnO/Al_2O_3 nanoparticles resulted in 98% MO adsorption, as shown in Fig. 13. According to this figure, MO peak decreases with increasing reaction time, while the intensity of the MB peak is almost constant. The initial adsorption of MB dye was less than 5%, which indicates the absence of any significant relationship between these two dyes with the catalyst. Furthermore, the observation of mixture color change confirms that only the blue MB color remains in the end.

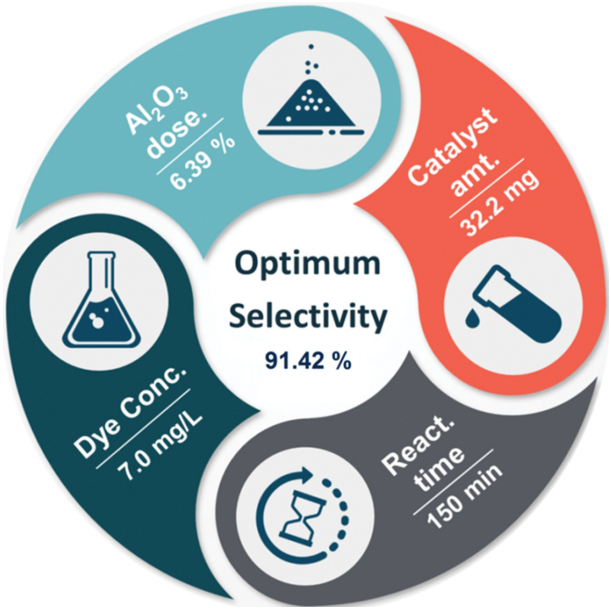

Fig. 12. The scheme of optimized output values by central composite design (CCD).

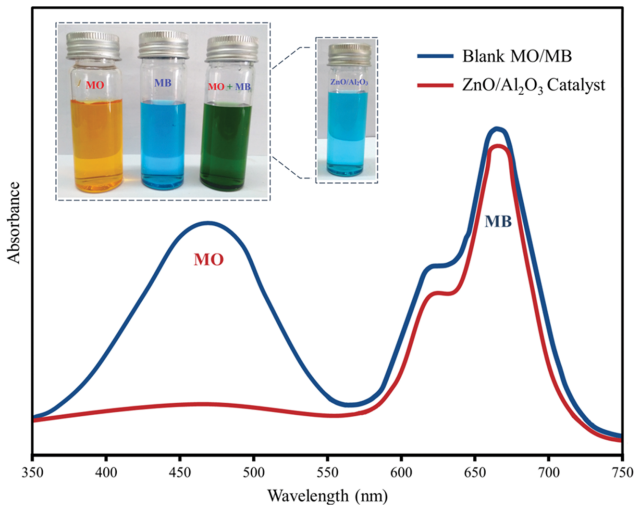

Fig. 13. The absorption spectra of MO removal in the mixture with MO and MB.

3. Selectivity Degradation

In the optimal conditions of selective removal, sono/photocatalytic process was used for MO degradation. FTIR spectroscopy was used for the qualitative determination of MO degradation. The FTIR spectra of Pure MO, ZnO/Al_2O_3, MO adsorbed and MO

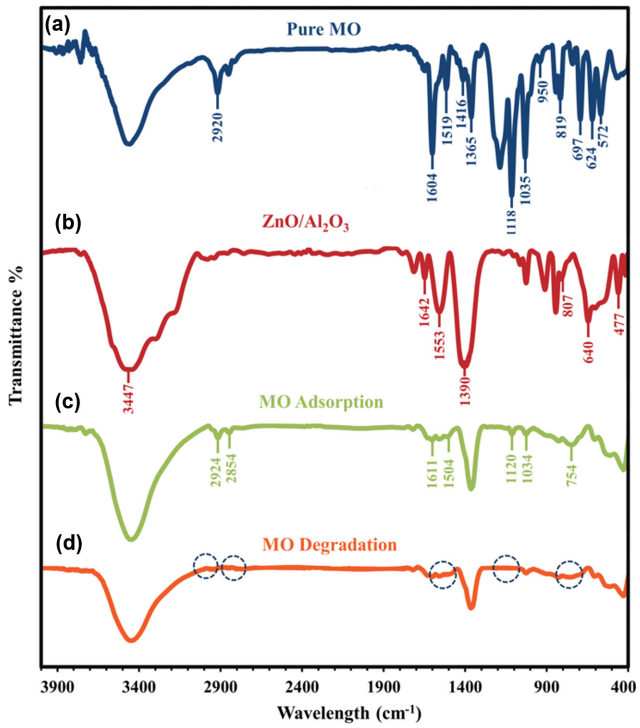

Fig. 14. The FTIR spectra of pure MO, ZnO/Al_2O_3 catalyst, MO adsorbed and MO degradation on the catalyst surface.

degraded on the catalyst are shown in Fig. 13. The FTIR spectra of Pure MO in Fig. 14(a) display a band at 819 cm^{-1} for the disubstituted benzene ring, bands at 847, 950, and 1,035 cm^{-1} for ring vibrations, bands at 1,416 and 1,519 cm^{-1} for C=C-H, and a band at 2,920 cm^{-1} for asymmetric CH_3 stretching vibrations. The band at 1,604 cm^{-1} for the N=N and the bands at 1,190 and 1,118 cm^{-1} for C-N verify the azo nature of the dye. The bands at a stretch 697, 624, and 572 cm^{-1} for C-S stretching vibrations and band at 1,365 cm^{-1} for S=O stretching vibrations verify the sulfonic nature of the MO. For comparison, the FTIR spectrum of ZnO/Al_2O_3 without dye molecules is shown in Fig. 14(b). The wide peak at 3,447 cm^{-1} corresponds to O-H stretching vibration, and other peaks at 1,390, 1,553 and 1,642 cm^{-1} belong to the C-O, C=O and CO_2 groups. As can be seen, the FTIR spectrum represents an absorption band at 477 cm^{-1} which is the characteristic absorption band of ZnO. Moreover, the two wide absorption peaks at 640 and 807 cm^{-1} correspond to Al-O stretching vibrations. Fig. 14(c) shows the adsorption of MO on the ZnO/Al_2O_3 surface. The bands of 754, 1,034, 1,120, 1,504, 1,611, 2,854 and 2,924 cm^{-1} are shown in the diagram indicate the presence of MO molecules in the catalyst structure. In Fig. 14(d), the FTIR spectrum of the MO degradation by sono/photocatalytic process shows complete removal of some bands compared to the initial control dye, which confirms the degradation of MO after UV and US radiation. According to the results, the bands of 754, 1,120, 1,504, 2,854 and 2,924 cm^{-1} were removed, representing the C-S, C-N, C=C-H and CH_3 bonds of MO, respectively. Many researches have been done to improve selective properties with advanced oxidation techniques. As mentioned, in this research, the ZnO/Al_2O_3 nanoparticles were synthesized by the relatively low-temperature ultrasound-assisted sol-gel method, with no template or surfactants. In most studies, TiO_2 NPs have been used as selective catalysts. According to these studies, so far, no studies have been performed on selective degradation of ZnO/Al_2O_3 catalysts with photochemical and sonochemical methods. When these two systems combine (sonophotocatalysis), the synergistic effect accelerates the catalytic degradation of organic compounds. Sonophotocatalysis is emerging as one of the most efficient treatment techniques for the degradation of pollutants of the aqueous medium. It is expected that progressive research will result from the most effective efficiency of degradation using these technologies. Table 6 represents the studies performed on selective degradation systems for MO/MB in comparison with the present study.

3-1. Sonocatalytic Activity Mechanism

The ultrasound phenomenon can be explained by the liquid cavitation mechanism, which causes a high temperature and local pressure in the reaction medium [43]. This process includes growth and finally collapse of a series of bubbles using ultrasound to the solution, which generates a shock wave [44]. Bubble growth is caused by the diffusion of solvent vapor into the bubble and continues until it collapses. The bubbles burst, release energy locally and allow chemical reactions to take place [45]. The principle of the energy release theory due to cavitation is based on the hot spot theory. According to this theory, the explosion of bubbles in the solution creates a very high local temperature [46]. The hot spots formed in the solution are very short-lived (less than 100 microseconds) and have a temperature of about 5,000 K and a pressure between 500 and 1,000 atm [47]. The bubble growth in liquids is generally spherical, but in liquids containing solids, the cavitation process is not spherical. When cavitation occurs near the solid surface, the

Table 6. Summary of the reported results for the selective removal of MO/MB

Author	Type catalyst	Pollutant	Conditions	Selective %
Liu [22]	TiO_2	MB/MO	UV Irradiation	53%
Lazar [27]	TiO_2	MB/MO	UV Irradiation	85%
Ye [25]	TiO_2	MB/MO	UV Irradiation	50%
Zhang [42]	TiO_2	MB/MO	UV Irradiation	85%
Zhang [26]	TiO_2	MB/MO	UV Irradiation	50%
Pakdel [23]	TiO_2/SiO_2	MB/MO	UV Irradiation	95%
Jose [24]	TiO_2	MB/MO	UV Irradiation	70%
Present study	ZnO/Al_2O_3	MB/MO	UV/US Combination	92%

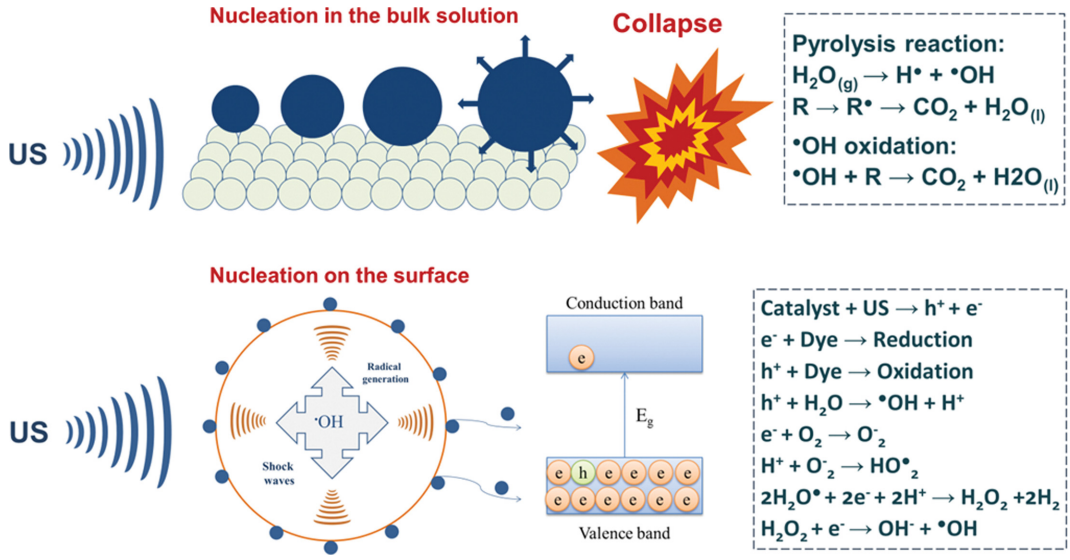

Fig. 15. The scheme of the sonocatalytic degradation mechanism.

bubbles collapse as a fountain and disperse the liquid from the surface at a very high rate. These collapse and shock waves are associated with them which act as micro-jets and capable of degrading the solid surface that is heated due to cavitation and hot spot formation [48]. In general, these reactions are performed through two mechanisms of primary and secondary sonochemistry. In primary sonochemistry, the initial reaction is performed in the collapsing bubble and then diffused into the reaction solution. While in secondary sonochemistry, active chemical species (radicals from the decomposition of compounds due to applying the ultrasound) form in the collapsing bubble that diffuses into the liquid phase and reacts with the solution raw materials to form the main product. In the sono/photocatalysis process, which is a combination of photocatalytic and sonocatalytic techniques, a significant synergy is observed to remove pollutants. This synergism is explained as follows:

1) Increased catalyst surface due to ultrasonic decomposition.

2) Improved mass transfer of compounds between the liquid phase and the catalyst surface.

3) Reduce charge recombination due to the production of more hydroxyl radicals H_2O_2.

4) Increased degradation efficiency due to the presence of catalyst particles that cause more bubbles to the formation.

The mechanism of sonocatalytic degradation is shown schematically in Fig. 15.

CONCLUSION

ZnO/Al_2O_3 nanocomposites were synthesized by the ultrasound-assisted. The effect of Al_2O_3 on structure, morphological, elemental compositions, absorption spectrum and selective sono/photocatalytic degradation was investigated. Due to increment of Al_2O_3 dosage, spherical and hexagonal structures were converted to flake-like quadrilateral morphology. The BET surface area of ZnO and ZnO/Al_2O_3 nanoparticles was obtained as 14.13 and 89.53 m^2/g, respectively. Based on the results, ZnO/Al_2O_3 nanoparticles were a very active catalyst for selective sono/photocatalytic degradation of MO dye in MO/MB aqueous solution. The results of ANOVA showed the proposed second-order polynomial model has good accuracy. This finding confirmed the reliability of the model and the good accuracy of the CCD method to optimize the selective removal of MO. The optimized determined variables for the selective removal efficiency of MO were found at the Al_2O_3 dosage of 6.39 wt%, catalyst amount of 32.2 mg, dye concentration of 7 mg/L, and reaction time of 150 min. In these conditions, the selective removal efficiency of MO was achieved equal to 90.06%. Afterward, sono/photocatalytic process was used for degradation of the adsorbed MO on the catalyst surface under optimum conditions. Based on the FTIR spectra, the use of a combination of photocatalytic and sonocatalytic processes had a good effect on MO degradation. Because of reactive oxygen species production such as superoxide radical anion, hydrogen peroxide (H_2O_2), hydroxyl radical (OH•) and oxygen (O_2•), MO dye molecules oxidize quickly. Furthermore, the use of semiconductor materials in sonocatalysis caused to produce electron/hole pairs, which consequently leads to more production of oxygen radicals.

REFERENCES

1. S. N. Rao and S. Shrivastava, *Mater. Today: Proceedings*, **29**, 1161 (2020).
2. A. Pandey, P. Singh and L. Iyengar, *Int. Biodeterior. Biodegrad.*, **59**, 73 (2007).
3 M. Botz, T. Mudder and A. Akcil, *Adv. Gold Ore Processing*, **4528**, 672 (2005).
4. F. Zhu, Y.-M. Zheng, B.-G. Zhang and Y.-R. Dai, *J. Hazard. Mater.*, **401**, 123608 (2021)
5. S. Karmakar, D. Roy and S. De, *Chem. Eng. J.*, **403**, 125103 (2021).
6. L. N. Griffiths and W. J. Mitsch, *Sci. Total Environ.*, **727**, 138337 (2020).
7. J. Díaz-Angulo, S. Cotillas, A. I. Gomes, S. M. Miranda, M. Mueses,

F. Machuca-Martínez, M. A. Rodrigo, R. A. Boaventura and V. J. Vilar, *Chemosphere*, **263**, 128049 (2021).
8. K. Manjari and A. K. Saroha, *J. Environ. Chem. Eng.*, **6**, 6256 (2018).
9. G. Mohanakrishna, R. I. Al-Raoush and I. M. Abu-Reesh, *Fuel*, **285**, 119104 (2021).
10. W. Qiu, W. Li, J. He, H. Zhao, X. Liu and Y. Yuan, *J. Environ. Sci.*, **74**, 177 (2018).
11. E. M. Cuerda-Correa, M. F. Alexandre-Franco and C. Fernández-González, *Water*, **12**, 102 (2020).
12. L. Liang, Y. Tursun, A. Nulahong, T. Dilinuer, A. Tunishaguli, G. Gao, A. Abulikemu and K. Okitsu, *Ultrason. Sonochem.*, **39**, 93 (2017).
13. Y. Peng, Z. Zhang, M. Wang, X. Shi, Y. Zhou, Y. Zhou and Y. Kong, *Ultrason. Sonochem.*, **69**, 105254 (2020).
14. T. G. McKenzie, F. Karimi, M. Ashokkumar and G. G. Qiao, *Chem.–A Eur. J.*, **25**, 5372 (2019).
15. R. Mohamed, D. McKinney and W. Sigmund, *Mater. Sci. Eng.: R: Rep.*, **73**, 1 (2012).
16. R. Mahdavi and S. S. Ashraf Talesh, *Int. J. Environ. Anal. Chem.*, 1 (2020).
17. M. Jafarzadeh, I. Rahman and C. Sipaut, *J. Sol-Gel Sci. Technol.*, **50**, 328 (2009).
18. H. Xu, B. W. Zeiger and K. S. Suslick, *Chem. Soc. Rev.*, **42**, 2555 (2013).
19. J. H. Bang and K. S. Suslick, *Adv. Mater.*, **22**, 1039 (2010).
20. F. M. Nowak, *Sonochemistry: Theory, reactions, syntheses, and applications*, Nova Science Publishers, New York (2010).
21. J. Kou, C. Lu, J. Wang, Y. Chen, Z. Xu and R. S. Varma, *Chem. Rev.*, **117**, 1445 (2017).
22. J. Liu, Z.-Y. Hu, Y. Peng, H.-W. Huang, Y. Li, M. Wu, X.-X. Ke, G. Van Tendeloo and B.-L. Su, *Appl. Catal. B: Environ.*, **181**, 138 (2016).
23. E. Pakdel, W. A. Daoud, S. Seyedin, J. Wang, J. M. Razal, L. Sun and X. Wang, *Colloids Surf. A: Physicochem. Eng. Aspects*, **552**, 130 (2018).
24. T. Jose, C. Vincent, K. Lilly and M. A. Lazar, *Mater. Today: Proceedings*, **9**, 21 (2019).
25. L. Ye, C. Yang, L. Tian, L. Zan and T. Peng, *Appl. Surf. Sci.*, **257**, 8072 (2011).
26. J. Zhang, W. Fu, J. Xi, H. He, S. Zhao, H. Lu and Z. Ji, *J. Alloys Compd.*, **575**, 40 (2013).
27. M. A. Lazar and W. A. Daoud, *RSC Adv.*, **2**, 447 (2012).
28. Y.-Y. Lau, Y.-S. Wong, T.-T. Teng, N. Morad, M. Rafatullah and S.-A. Ong, *RSC Adv.*, **5**, 34206 (2015).
29. D. C. Montgomery, *Design and analysis of experiments*, John Wiley & Sons, New Jersey (2017).
30. O. V. Okoro, Z. Sun and J. Birch, *Thermal depolymerization of biogas digestate as a viable digestate processing and resource recovery strategy*, in: Advances in eco-fuels for a sustainable environment, Advances in eco-fuels for a sustainable environment. Woodhead Publishing, Sawston (2019).
31. N. Brezhneva, N. V. Dezhkunov, S. A. Ulasevich and E. V. Skorb, *Ultrason. Sonochem.*, **70**, 105315 (2021).
32. H. Tajizadegan, O. Torabi, A. Heidary, M. H. Golabgir and A. Jamshidi, *Desalination and Water Treatment*, **57**, 12324 (2016).
33. E. Alian, A. Semnani, A. Firooz, M. Shirani and B. Azmoon, *Arabian J. Sci. Eng.*, **43**, 229 (2018).
34. A. Almasi, S. A. Mousavi, Z. Bahman, M. R. Zolfaghari and A. A. Zinatizadeh, *Desalination and Water Treatment*, **57**, 23589 (2016).
35. N. Mandal, B. Doloi and B. Mondal, *Int. J. Precision Eng. Manufacturing*, **13**, 1589 (2012).
36. A. Almasi, M. Mohammadi, F. Baniamerian, Z. Berizi, M. Almasi and Z. Pariz, *Int. J. Environ. Sci. Technol.*, **16**, 8437 (2019).
37. M. Papadaki, R. J. Emery, M. A. Abu-Hassan, A. Díaz-Bustos, I. S. Metcalfe and D. Mantzavinos, *Sep. Purif. Technol.*, **34**, 35 (2004).
38. S. Piri, N. Mehranbod, M. Moussavi and S. M. Mirsoleimani-azizi, *Int. J. Environ. Sci. Technol.*, **17**, 321 (2020).
39. R. Boppella, K. Anjaneyulu, P. Basak and S. V. Manorama, *J. Phys. Chem. C*, **117**, 4597 (2013).
40. K. Haitham, S. Razak and M. Nawi, *Arabian J. Chem.*, **12**, 1595 (2019).
41. R. Mahdavi and S. S. A. Talesh, *Adv. Powder Technol.*, **28**, 1418 (2017).
42. J. Zhang, W. Chen, J. Xi and Z. Ji, *Mater. Lett.*, **79**, 259 (2012).
43. R. Mahdavi and S. S. A. Talesh, *Ultrason. Sonochem.*, **51**, 230 (2019).
44. K. Peng, F. G. Qin, R. Jiang and S. Kang, *Ultrason. Sonochem.*, **69**, 105253 (2020).
45. C. Zhao, Y. Zhang, H. Cao, X. Zheng, T. Van Gerven, Y. Hu and Z. Sun, *Ultrason. Sonochem.*, **52**, 484 (2019).
46. J. M. Costa and A. F. de Almeida Neto, *Ultrason. Sonochem.*, **68**, 105193 (2020).
47. B. G. Pollet and M. Ashokkumar, *Fundamental and applied aspects of ultrasonics and sonochemistry*, in: Introduction to Ultrasound, Sonochemistry and Sonoelectrochemistry, SpringerBriefs in Molecular Science, Springer, Berlin (2019).
48. R. Mahdavi and S. S. A. Talesh, *Ultrason. Sonochem.*, **39**, 504 (2017).